

# A tunable topological insulator in the spin helical Dirac transport regime

D. Hsieh<sup>1</sup>, Y. Xia<sup>1</sup>, D. Qian<sup>1,5</sup>, L. Wray<sup>1</sup>, J. H. Dil<sup>6,7</sup>, F. Meier<sup>6,7</sup>, J. Osterwalder<sup>7</sup>, L. Patthey<sup>6</sup>, J. G. Checkelsky<sup>1</sup>, N. P. Ong<sup>1</sup>, A. V. Fedorov<sup>8</sup>, H. Lin<sup>9</sup>, A. Bansil<sup>9</sup>, D. Grauer<sup>2</sup>, Y. S. Hor<sup>2</sup>, R. J. Cava<sup>2</sup> & M. Z. Hasan<sup>1,3,4</sup>

Helical Dirac fermions—charge carriers that behave as massless relativistic particles with an intrinsic angular momentum (spin) locked to its translational momentum—are proposed to be the key to realizing fundamentally new phenomena in condensed matter physics<sup>1–9</sup>. Prominent examples include the anomalous quantization of magneto-electric coupling<sup>4–6</sup>, half-fermion states that are their own antiparticle<sup>7,8</sup>, and charge fractionalization in a Bose–Einstein condensate<sup>9</sup>, all of which are not possible with conventional Dirac fermions of the graphene variety<sup>10</sup>. Helical Dirac fermions have so far remained elusive owing to the lack of necessary spin-sensitive measurements and because such fermions are forbidden to exist in conventional materials harbouring relativistic electrons, such as graphene<sup>10</sup> or bismuth<sup>11</sup>. It has recently been proposed that helical Dirac fermions may exist at the edges of certain types of topologically ordered insulators<sup>3,4,12</sup>—materials with a bulk insulating gap of spin–orbit origin and surface states protected against scattering by time-reversal symmetry—and that their peculiar properties may be accessed provided the insulator is tuned into the so-called topological transport regime<sup>3–9</sup>. However, helical Dirac fermions have not been observed in existing topological insulators<sup>13–18</sup>. Here we report the realization and characterization of a tunable topological insulator in a bismuth-based class of material by combining spin-imaging and momentum-resolved spectroscopies, bulk charge compensation, Hall transport measurements and surface quantum control. Our results reveal a spin-momentum locked Dirac cone carrying a non-trivial Berry's phase that is nearly 100 per cent spin-polarized, which exhibits a tunable topological fermion density in the vicinity of the Kramers point and can be driven to the long-sought topological spin transport regime. The observed topological nodal state is shown to be protected even up to 300 K. Our demonstration of room-temperature topological order and non-trivial spin-texture in stoichiometric Bi<sub>2</sub>Se<sub>3</sub>-M<sub>x</sub> (M<sub>x</sub> indicates surface doping or gating control) paves the way for future graphene-like studies of topological insulators, and applications of the observed spin-polarized edge channels in spintronic and computing technologies possibly at room temperature.

Unlike conventional Dirac fermions as in graphene, helical Dirac fermions possess a net spin and are guaranteed to be conducting because of time-reversal symmetry<sup>2–5</sup>, allowing the unique possibility of carrying spin currents without heat dissipation. However, the most important difference and a more exciting frontier lies in the topological properties of helical Dirac fermion systems<sup>3–5,12</sup>, which are expected to manifest in several ways, provided that the system can be tuned to the topological transport regime where the charge density vanishes (analogous to the charge neutrality point in graphene<sup>10,19</sup>).

These manifestations include an anomalous half-integer quantization of Hall conductance<sup>3–6</sup>, a realization of Majorana fermions (particles with anyon exchange statistics that differs from the conventional Bose or Fermi–Dirac statistics)<sup>7,8</sup>, and generation of fractionally charged quantum particles<sup>9</sup>. Helical fermions are believed to exist on the edges of certain types of three-dimensional (3D) topological insulators<sup>3,4,12</sup>, with material candidates Bi<sub>2</sub>X<sub>3</sub> (X = Se, Te)<sup>15</sup> recently proposed on the basis of observations<sup>15,17</sup> and models<sup>15,20</sup>. However, these materials cannot be used to detect helical Dirac fermion physics for three reasons. First, the helical properties of the surface electrons are unknown and depend on the materials' class. Second, their electronic structure is not in the topological transport regime, thus not allowing any of the interesting topological insulator experiments to be performed to date. Third, unlike two-dimensional (2D) quantum Hall Dirac systems such as graphene<sup>10,19</sup>, 3D topological insulators cannot be very easily tuned to this zero carrier density regime through standard electrical gating, which has prevented a revolution like that witnessed for graphene<sup>10</sup> from taking place for topological insulators<sup>2</sup>.

To determine the key helical properties of the edge electrons near the Fermi energy ( $E_F$ ) in our previously proposed candidate Bi<sub>2</sub>X<sub>3</sub> class<sup>15</sup>, we performed spin- and angle-resolved photoemission spectroscopy (spin-ARPES) scans using a double Mott detector set-up<sup>21</sup>, which systematically measures all three components of the spin of the electron as a function of its energy and momentum throughout the Brillouin zone (Supplementary Information). Although the surface electrons of both Bi<sub>2</sub>Se<sub>3</sub> and Bi<sub>2</sub>Te<sub>3</sub> exhibit a finite density of states near  $E_F$  (Fig. 1a–d), there is an additional contribution to the density of states around momentum  $\bar{\Gamma}$  from the spin-degenerate bulk conduction band in Bi<sub>2</sub>Se<sub>3</sub>. Therefore, the helical nature of the surface electrons is most clearly resolved in Bi<sub>2</sub>Te<sub>3</sub>. We analysed the spin-polarization of photoelectrons emitted at a binding energy  $E_B = -20$  meV along the  $k_x$  ( $\parallel \bar{\Gamma} - \bar{M}$ ) cut in Bi<sub>2</sub>Te<sub>3</sub> (Fig. 1e inset). Because the surface state dispersion of Bi<sub>2</sub>X<sub>3</sub> exhibits a pronounced time dependence after cleavage (Supplementary Information) related to semiconductor band bending and topological charging effects<sup>17</sup>, data collection times were only long enough to ensure a level of statistics sufficient to measure the spin-polarized character of the surface states.

Figure 1e and f shows the measured spin polarization spectra  $P_i$  of the  $i = x, y$  and  $z$  (out-of-plane) components along the  $\bar{\Gamma} - \bar{M}$  direction. In the  $x$  and  $z$  directions, no clear signal can be discerned within the margins of statistical error. In the  $y$  direction on the other hand, clear polarization signals of equal magnitude and opposite sign are observed for surface-edge electrons of opposite momentum, evidence that the spin and momentum directions are one-to-one

<sup>1</sup>Joseph Henry Laboratories of Physics, Department of Physics, <sup>2</sup>Department of Chemistry, <sup>3</sup>Princeton Center for Complex Materials, <sup>4</sup>Princeton Institute for Science and Technology of Materials, Princeton University, Princeton, New Jersey 08544, USA. <sup>5</sup>Department of Physics, Shanghai Jiao Tong University, Shanghai 200030, China. <sup>6</sup>Swiss Light Source, Paul Scherrer Institute, CH-5232, Villigen, Switzerland. <sup>7</sup>Physik-Institute, Universität Zürich-Irchel, 8057 Zürich, Switzerland. <sup>8</sup>Advanced Light Source, Lawrence Berkeley Laboratory, Berkeley, California 94720, USA. <sup>9</sup>Department of Physics, Northeastern University, Boston, Massachusetts 02115, USA.

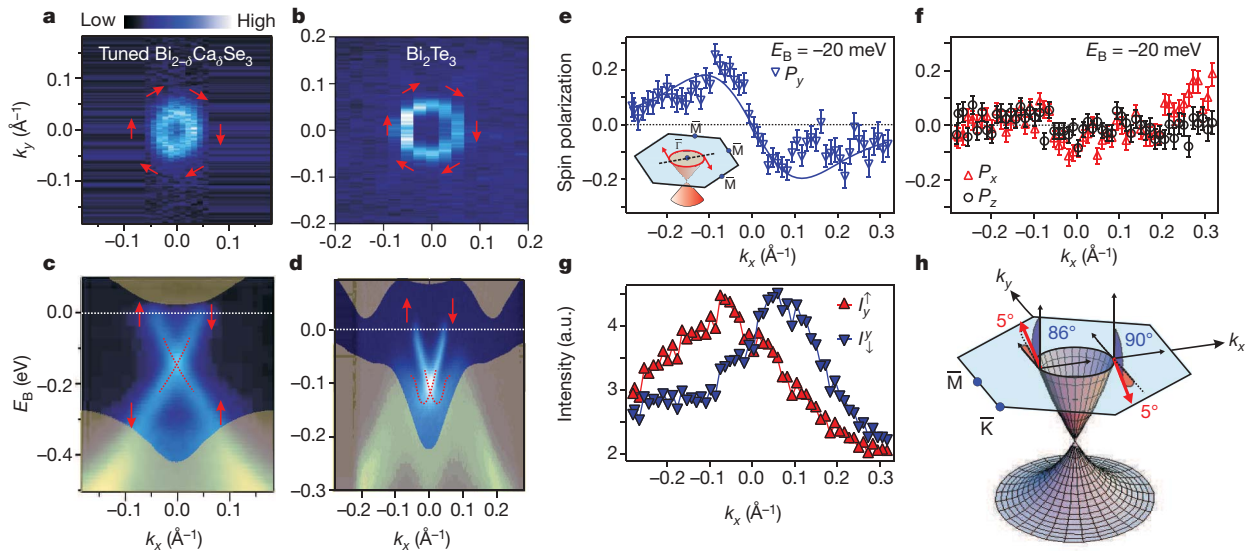


**Figure 1 | Detection of spin-momentum locking of spin-helical Dirac electrons in  $\text{Bi}_2\text{Se}_3$  and  $\text{Bi}_2\text{Te}_3$  using spin-resolved ARPES.** **a, b**, ARPES intensity map at  $E_F$  of the (111) surface of tuned stoichiometric  $\text{Bi}_{2-\delta}\text{Ca}_\delta\text{Se}_3$  (**a**; see text) and of  $\text{Bi}_2\text{Te}_3$  (**b**). Red arrows denote the direction of spin projection around the Fermi surface. **c, d**, ARPES dispersion of tuned  $\text{Bi}_{2-\delta}\text{Ca}_\delta\text{Se}_3$  (**c**) and  $\text{Bi}_2\text{Te}_3$  (**d**) along the  $k_x$  cut. The dotted red lines are guides to the eye. The shaded regions in **c** and **d** are our projections of the bulk bands of pure  $\text{Bi}_2\text{Se}_3$  and  $\text{Bi}_2\text{Te}_3$ , respectively, onto the (111) surface. **e**, Measured  $y$  component of spin-polarization along the  $\bar{\Gamma}-\bar{M}$  direction at  $E_B = -20$  meV, which only cuts through the surface states. Inset, schematic of the cut direction. **f**, Measured  $x$  (red triangles) and  $z$  (black circles) components of spin-polarization along the  $\bar{\Gamma}-\bar{M}$  direction at

$E_B = -20$  meV. Error bars in **e** and **f** denote the standard deviation of  $P_{x,y,z}$  where typical detector counts reach  $5 \times 10^5$ ; solid lines are numerical fits<sup>21</sup>. **g**, Spin-resolved spectra obtained from the  $y$  component spin polarization data. The non-Lorentzian lineshape of the  $I_y^\uparrow$  and  $I_y^\downarrow$  curves and their non-exact merger at large  $|k_x|$  is due to the time evolution of the surface band dispersion, which is the dominant source of statistical uncertainty. a.u., arbitrary units. **h**, Fitted values of the spin polarization vector  $\mathbf{P}$  ( $S_x, S_y, S_z$ ) are  $(\sin 90^\circ \cos -95^\circ, \sin 90^\circ \sin -95^\circ, \cos 90^\circ)$  for electrons with  $+k_x$  and  $(\sin 86^\circ \cos 85^\circ, \sin 86^\circ \sin 85^\circ, \cos 86^\circ)$  for electrons with  $-k_x$ , which demonstrates the topological helicity of the spin-Dirac cone. The angular uncertainties are of the order of  $\pm 10^\circ$  and the magnitude uncertainty is of the order of  $\pm 0.15$ .

locked due to  $Z_2$  topology. This is most clearly seen in the spin-resolved spectra ( $I_y^{\uparrow,\downarrow}$ ; Fig. 1g), which are calculated from  $P_y$  according to  $I_y^\uparrow = I_{\text{tot}}(1 + P_y)/2$  and  $I_y^\downarrow = I_{\text{tot}}(1 - P_y)/2$ , where  $I_{\text{tot}}$  is the spin-averaged intensity. To extract the spin polarization vectors of the forward ( $+k_x$ ) and backward ( $-k_x$ ) moving electrons, we performed a standard numerical fit (Supplementary Information)<sup>21</sup>. The fit results yield  $100(\pm 15)\%$  polarized (Fig. 1h) spins that point along the  $(\mathbf{k} \times \mathbf{z})$  direction, which is consistent with its topological spin-orbit coupling origin<sup>14,21</sup>. Spin-momentum locking is the key to topological order in a topological insulator which cannot be demonstrated without spin sensitive detection. Therefore the existence of the topological insulator state was not established in previous work on  $\text{Bi}_2\text{X}_3$ . Our combined observations of a spin-orbit origin linear dispersion relation and a one-to-one locking of momentum and spin directions allow us to conclude that the surface electrons of  $\text{Bi}_2\text{X}_3$  ( $X = \text{Se}, \text{Te}$ ) are helical Dirac fermions of  $Z_2$  topological-order origin (Fig. 1).

To experimentally access these helical Dirac fermions for research-device applications, the electronic structure must be in the topological transport regime where there is zero charge fermion density<sup>7-9</sup>. This regime occurs when  $E_F$  lies in between the bulk valence band maximum (VBM) and the bulk conduction band minimum (CBM), and exactly at the surface or edge Dirac point, which should in turn lie at a Kramers time-reversal invariant momentum<sup>3,4</sup>. This is clearly not the case in either  $\text{Bi}_2\text{Te}_3$ ,  $\text{Bi}_2(\text{Sn})\text{Te}_3$ ,  $\text{Bi}_2\text{Se}_3$  or graphene. Although pure  $\text{Bi}_2\text{X}_3$  are expected to be undoped semiconductors<sup>20,22,23</sup>, nominally stoichiometric samples are well known to be n- and p-type semiconductors owing to excess carriers introduced via Se or Te site defects, respectively<sup>16,17</sup>. To compensate for the unwanted defect dopants, trace amounts of carriers of the opposite sign must be added into the naturally occurring material, which may be easier to achieve in  $\text{Bi}_2\text{Se}_3$  than in  $\text{Bi}_2\text{Te}_3$  because the former has a much larger bandgap<sup>15,24</sup> (around 0.35 eV (ref. 25) compared to 0.18 eV (ref. 26), respectively). To lower the  $E_F$  of  $\text{Bi}_2\text{Se}_3$  into the bulk bandgap, we

substituted trace amounts of  $\text{Ca}^{2+}$  for  $\text{Bi}^{3+}$  in as-grown  $\text{Bi}_2\text{Se}_3$ , where Ca has been previously shown<sup>16</sup> to act as a hole donor by scanning tunnelling microscopy and thermoelectric transport studies<sup>16</sup>. Figure 2a shows that as the Ca concentration increases from 0% to 0.5%, the low temperature resistivity sharply peaks at 0.25%, which suggests that the system undergoes a metal to insulator to metal transition. The resistivity peak occurs at a Ca concentration where a change in sign of the Hall carrier density also is observed (Fig. 2b), which shows that for measured Ca concentrations below and above 0.25%, electrical conduction is supported by electron and hole carriers, respectively.

We performed systematic time-dependent ARPES measurements to study the electronic structure evolution of  $\text{Bi}_{2-\delta}\text{Ca}_\delta\text{Se}_3$  as a function of Ca doping in order to gain insight into the trends observed in transport (Fig. 2a and b). Early time ARPES energy dispersion maps taken through the  $\bar{\Gamma}$  point of the (111) surface Brillouin zone are displayed in Fig. 2c-h for several Ca doping levels. In the as-grown ( $\delta = 0$ )  $\text{Bi}_2\text{Se}_3$  samples, a single surface Dirac cone is observed with  $E_F$  lying nearly 0.3 eV above the Dirac node forming an electron Fermi surface. We also observe that  $E_F$  intersects the electron-like bulk conduction band. When a 0.25% concentration of Ca is introduced,  $E_F$  is dramatically lowered to lie near the Dirac node (Fig. 2d), which is consistent with Ca acting as a highly effective hole donor. Because the bulk CBM lies at a binding energy of approximately -0.1 eV for  $\delta = 0$  (Fig. 2c), a 0.3 eV shift in  $E_F$  between  $\delta = 0$  and  $\delta = 0.0025$  suggests that for  $\delta = 0.0025$ ,  $E_F$  is located 0.2 eV below the CBM. This is consistent with  $E_F$  being in the bulk bandgap, because the indirect energy gap between the CBM and the VBM is known from both tunnelling<sup>24</sup> and optical<sup>25</sup> data and theory<sup>22</sup> to be nearly 0.35 eV.

As the Ca concentration is increased further, the position of  $E_F$  continues a downward trend such that by  $\delta = 0.01$ , it is located clearly below the Dirac node (Fig. 2) and intersects the hole-like bulk valence band. The systematic lowering of  $E_F$  with increasing  $\delta$  in  $\text{Bi}_{2-\delta}\text{Ca}_\delta\text{Se}_3$  observed in early time ARPES measurements (Fig. 2i-k), which reflect the electronic structure of the sample bulk,

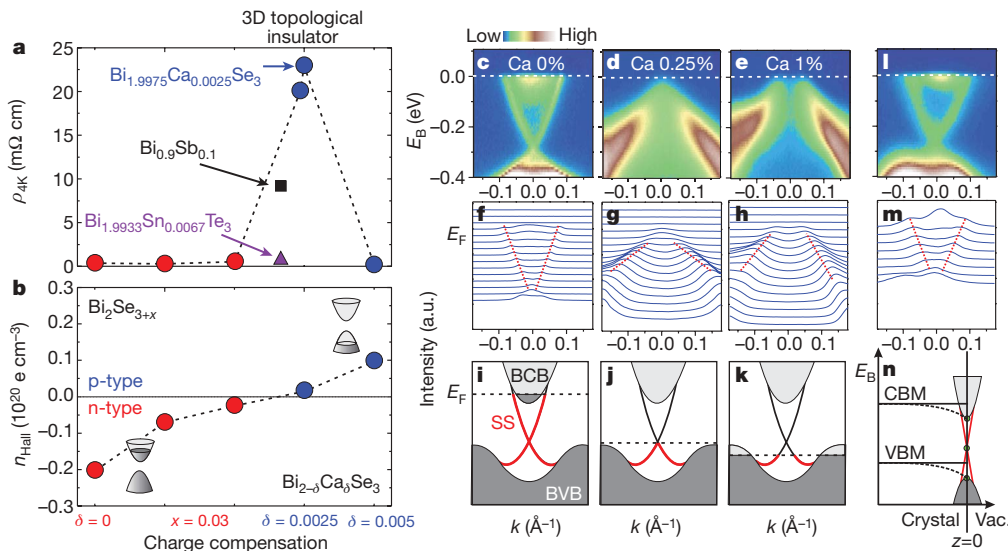


**Figure 2 | Tuning the bulk Fermi level through systematic bulk charge compensation monitored through systematic transport and ARPES measurements.** **a**, Resistivity at  $T = 4\text{ K}$  measured for samples of  $\text{Bi}_2\text{Se}_3$  (filled circles, no arrow labels) that are bulk electron doped due to varying concentrations of Se vacancies<sup>16</sup> ( $x$ ) or bulk hole doped through Ca/Bi substitution ( $\delta$ ). These are compared to analogous values for the topological insulators  $\text{Bi}_{0.9}\text{Sb}_{0.1}$  (black square, arrowed; ref. 13) and  $\text{Bi}_{1.9933}\text{Sn}_{0.0067}\text{Te}_3$  (purple triangle, arrowed). The stoichiometric  $\text{Bi}_2\text{Se}_3$  ( $\text{Bi}_{1.9975}\text{Ca}_{0.0025}\text{Se}_3$ ) is found to be the most insulating of these topological insulators. In  $\text{Bi}_2(\text{Ca})\text{Se}_3$ , bulk resistivity in excess of  $75\text{ m}\Omega\text{ cm}$  is possible, which will be shown elsewhere. The bulk insulating state in  $\text{Bi}_{0.9}\text{Sb}_{0.1}$  (ref. 13) is intrinsic and not due to disorder which will also be shown elsewhere.  $\text{Bi}_{1.9933}\text{Sn}_{0.0067}\text{Te}_3$  is known to be most metallic-like among the three classes

studied so far. **b**, Hall carrier density of the same samples determined using Hall measurements. Symbols in **a** and **b** coloured red (blue) represent  $n$ - ( $p$ -) type behaviour. **c–e**, ARPES band dispersion images of  $\text{Bi}_{2-\delta}\text{Ca}_\delta\text{Se}_3$  (111) through  $\Gamma$  collected within 20 min after cleavage for  $\delta = 0$  (**c**),  $\delta = 0.0025$  (**d**) and  $\delta = 0.01$  (**e**). **f–h**, Corresponding momentum distribution curves. Red lines are guides to the eye. **i–k**, Schematic downward evolution of  $E_F$  with increasing Ca content. The occupied bulk conduction band (BCB) and bulk valence band (BVB) states are shaded dark, and the occupied surface states (SS) are coloured red. **l**, Typical ARPES band dispersion image of **c–e** taken around 18 h after cleavage, and **m**, its corresponding momentum distribution curves. **n**, Schematic of the surface band bending process that is responsible for the observed downward shift in energies over time. Vac., vacuum.

consistently explain the measured transport behaviour. However, we observe that  $E_F$  rises back up over time across all samples, such that all spectra relax back to a  $\delta = 0$  like spectrum on a typical timescale of 18 h (Fig. 2l). Such a slow upward shift of the surface Fermi level has also been observed in  $\text{Bi}_2\text{Te}_3$  (ref. 17) and is due to a surface band bending effect commonly observed in many semiconductors (Supplementary Information). Therefore, although bulk Ca doping succeeds in tuning  $E_F$  between the bulk valence and conduction bands, it does not change the position of  $E_F$  relative to the surface Dirac point in the ground state.

Because the surface Dirac point in the ground state of most insulating compound studied, stoichiometric  $\text{Bi}_2\text{Se}_3$  or  $\text{Bi}_{1.9975}\text{Ca}_{0.0025}\text{Se}_3$ , lies  $\sim 0.3\text{ eV}$  below  $E_F$ , its electronic structure is still not in the much desired topological quantum transport regime. To bring the surface Dirac point level with  $E_F$  in  $\text{Bi}_{2-\delta}\text{Ca}_\delta\text{Se}_3$ , we demonstrate here that hole carriers can be remarkably systematically introduced into the surface of a large-gap topological insulator by dosing with  $\text{NO}_2$  molecules, which has been previously known to work in non-insulating materials<sup>27,28</sup>. Figure 3 shows that with increasing surface hole donor concentration, the binding energy of the surface Dirac point rises monotonically towards  $E_F$ . Starting from  $E_B \approx -0.3\text{ eV}$  at a dose of 0 Langmuir (0 L; refs 27, 28), it rises to  $-0.15\text{ eV}$  at 0.1 L where the surface bent CBM has completely disappeared, and finally to the charge neutrality point ( $E_B = 0\text{ eV}$ ) at 2 L. No further changes of the chemical potential are observed with higher dosages. To quantify the surface carrier density ( $n$ ) dependence on surface hole donor concentration, we mapped the surface state Fermi surface in Fig. 3a–c and performed a Luttinger electron count (number density on the surface) based on Fermi surface area,  $n = A_{FS}/A_{BZ}$ , where  $A_{FS}$  is the area of the Fermi surface and  $A_{BZ}$  is the area of the surface Brillouin zone. We find that 0.1 L of  $\text{NO}_2$  removes approximately 0.0066 electrons per surface unit cell of  $\text{Bi}_{2-\delta}\text{Ca}_\delta\text{Se}_3$  (111), and an excess of 2 L reduces the Fermi surface to a single point within our experimental resolution, which has an additional 0.005 electrons per unit cell

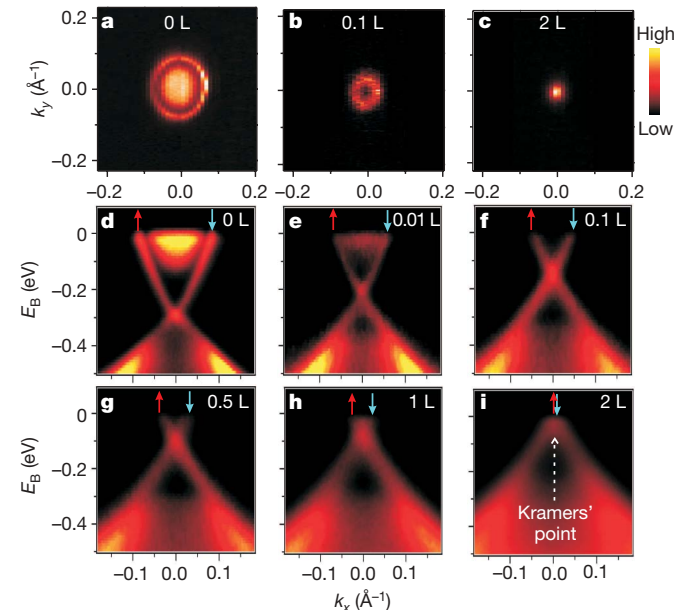


**Figure 3 | Tuning the density of helical Dirac electrons to the spin-degenerate Kramers point and topological transport regime.** **a**, A high resolution ARPES mapping of the topological surface Fermi surface near  $\Gamma$  of  $\text{Bi}_{2-\delta}\text{Ca}_\delta\text{Se}_3$  (111). The diffuse intensity within the ring originates from the bulk-surface resonance state<sup>15</sup>. **b**, The Fermi surface after 0.1 L of  $\text{NO}_2$  is dosed, showing that the resonance state is removed. **c**, The Fermi surface after a 2 L dosage, which achieves the Dirac charge neutrality point. **d–i**, High resolution ARPES surface band dispersions through  $\Gamma$  after an  $\text{NO}_2$  dosage (L) of 0 (**d**), 0.01 (**e**), 0.1 (**f**), 0.5 (**g**), 1 (**h**) and 2 (**i**). The arrows denote the topological spin polarization of the bands. We note that owing to an increasing level of surface disorder with  $\text{NO}_2$  adsorption, the measured spectra become progressively more diffuse and the total photoemission intensity from the buried  $\text{Bi}_{2-\delta}\text{Ca}_\delta\text{Se}_3$  surface is gradually reduced.

removed. Because surface doping does not affect the carrier density in the bulk (which thus remains insulating), the energy of the Dirac point is lifted above the bulk VBM: a new time independent electronic ground state is realized that lies in the topological transport regime with  $E_F$  intersecting the Dirac node.

In order to investigate the thermal stability and strength of topological order of this nodal Dirac ground state (Fig. 4e), temperature dependent ARPES scans were collected on  $\text{Bi}_{2-\delta}\text{Ca}_\delta\text{Se}_3$  samples that were first surface hole doped with  $\text{NO}_2$  at a temperature  $T = 10$  K. Figure 4c and d illustrates that the charge neutral point-like Fermi surface (Fig. 4a) is robust up to room temperature ( $T = 300$  K) over measurement times of days. A density of states that decreases linearly to zero at the Dirac point energy at 300 K (Fig. 4f) is further evidence that the low energy properties of stoichiometric  $\text{Bi}_2\text{Se}_3$ ,  $\text{NO}_2$  or  $\text{Bi}_{1.9975}\text{Ca}_{0.0025}\text{Se}_3$ ,  $\text{NO}_2$  are dominated by a novel topological ground state that features massless helical Dirac fermions with nearly 100% spin polarization. This also confirms a non-trivial  $\pi$  Berry's phase on the surface due to the spin-momentum locking pattern that we observed which is similar to the robust Berry's phase previously observed in the Bi-Sb system<sup>14</sup> (Fig. 1).

Helical nodal Dirac fermions are forbidden from acquiring a mass through bandgap formation because they are located around time-reversal invariant (Kramers') momenta  $k_T = \bar{\Gamma}$  or  $\bar{M}$  (Fig. 4h). This makes them fundamentally different from chiral Dirac fermions such as those found in graphene, which are located at  $\bar{K}$  and not topologically protected (Fig. 4g) and can develop an undesirable mass while in contact with a substrate. The helical nodal Dirac fermion on the surface of  $\text{Bi}_2\text{Se}_3$  owes its existence to a non-zero topological number  $\nu_0$  given by  $(-1)^{\nu_0} = \prod_{k_T} \prod_{m=1}^N \xi_{2m}(k_T)$ , where  $\xi_{2m}(k_T)$  is the parity eigenvalue of the bulk wavefunction at the 3D Kramers' point  $k_T$  and  $N$  is the number of occupied bulk bands<sup>4</sup>. Because Ca dopants are present in only trace quantities in  $\text{Bi}_{1.9975}\text{Ca}_{0.0025}\text{Se}_3$ ,  $\text{NO}_2$ , the values of  $\xi_{2m}(k_T)$  do not deviate from those of  $\text{Bi}_2\text{Se}_3$ , as evidenced by the persistence of a single gapless surface band in both naturally grown  $\text{Bi}_2\text{Se}_3$  and  $\text{Bi}_{1.9975}\text{Ca}_{0.0025}\text{Se}_3$ . Both  $\text{Ca}^{2+}$  and  $\text{NO}_2^-$  are non-magnetic and so do not break time-reversal symmetry, therefore the same topological quantum number ( $\nu_0 = 1$ ) applies in the Dirac

transport regime (Fig. 4) realized by our method shown here, which is stable with both time and temperature. Our direct demonstration of spin-polarized edge channels and room temperature operability of chemically gated stoichiometric  $\text{Bi}_2\text{Se}_3$  or  $\text{Bi}_{2-\delta}\text{Ca}_\delta\text{Se}_3$ ,  $\text{NO}_2$ , not achieved in purely 2D topological systems such as Hg(Cd)Te quantum wells<sup>29</sup>, enables exciting future room temperature experiments on surface helical Dirac fermions that carry non-trivial  $\pi$  Berry's phase.

Our demonstration of topological order at room temperature opens up possibilities of using quantum Hall-like phenomena and spin-polarized protected edge channels for spintronic or computing device applications without the traditional requirements of high magnetic fields and delicate cryogenics. A direct detection of surface-edge states would be possible in stoichiometric  $\text{Bi}_2\text{Se}_3$  or  $\text{Bi}_{2-\delta}\text{Ca}_\delta\text{Se}_3$ , using transport methods which will bear signatures of weak anti-localization and thus exhibit anomalous magneto-optic effects. Here we envisage a few sample experiments that could be carried out by using surface doped or electrically gated  $\text{Bi}_{2-\delta}\text{Ca}_\delta\text{Se}_3$ . By applying a weak time-reversal breaking perturbation at the helical surface so as to lift the Kramers degeneracy at  $E_F$  (a method of gap opening on the surface is shown in Supplementary Information), a half-integer quantized magneto-electric coupling can be realized<sup>3-6</sup>, which could be measured by standard quantum Hall probes. This would enable a variety of novel surface quantum Hall physics to be realized. Another class of experiments would be made possible by interfacing the helical topological surface with magnetic and ordinary superconducting films. An interferometer device could be built based on  $\text{Bi}_{2-\delta}\text{Ca}_\delta\text{Se}_3$  to create and detect long-sought Majorana fermions<sup>7,8</sup>. These particles, which have never been observed, possess only half the degrees of freedom of a conventional fermion and constitute the key building block for topological quantum computing that can operate in a fault-tolerant mode. Yet another class of experiments would be made possible by sandwiching a charge neutral topological insulator film made of  $\text{Bi}_{2-\delta}\text{Ca}_\delta\text{Se}_3$  within a charged capacitor. In this way, a microchip that supports a topological electron-hole condensate with fractional vortices<sup>9</sup> could be fabricated, which offers the exciting opportunity to probe

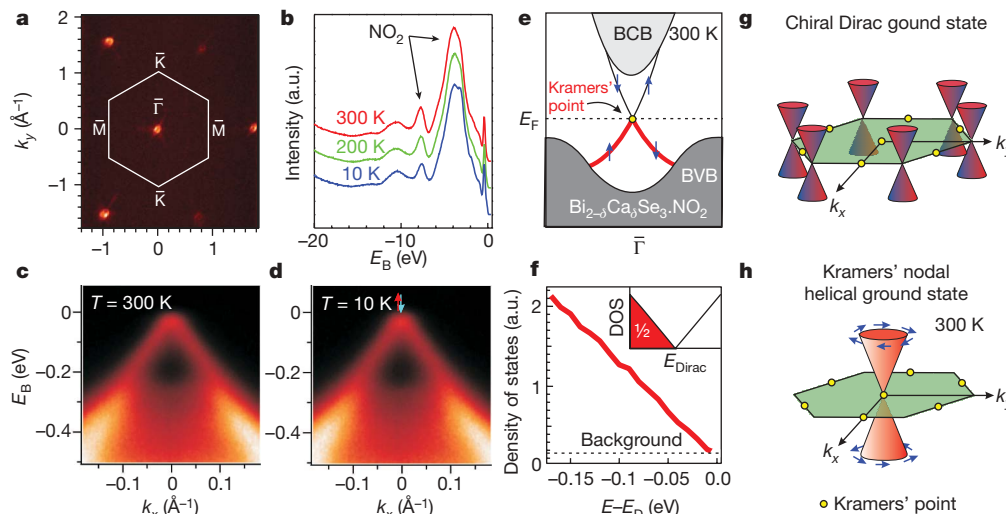


**Figure 4 | Topological order of the nodal helical Dirac ground state at 300K.** **a**, Typical ARPES intensity map of the  $\text{Bi}_2(\text{Se/Te})_3$  class collected at  $E_F$  spanning several Brillouin zones. **b**, Energy distribution curves of the valence bands of  $\text{Bi}_{2-\delta}\text{Ca}_\delta\text{Se}_3$  taken at  $T = 10$  K, 200 K and 300 K. The peaks around  $-4$  eV and  $-7.5$  eV come from  $\text{NO}_2$  adsorption (Supplementary Information). The intensity of these  $\text{NO}_2$  core level peaks do not change over this temperature range, indicating no measurable  $\text{NO}_2$  desorption during the heating process. **c**, **d**, ARPES intensity map of the surface state band dispersion of  $\text{Bi}_{2-\delta}\text{Ca}_\delta\text{Se}_3$  (111) after a 2 L dosage of  $\text{NO}_2$  is applied at  $T = 10$  K, which is taken at 300 K (**c**) and 10 K (**d**). **e**, Schematic of the surface

and bulk electronic structure of  $\text{Bi}_{2-\delta}\text{Ca}_\delta\text{Se}_3$ ,  $\text{NO}_2$ , tuned to the topological transport regime. **f**, Angle-integrated intensity near  $\bar{\Gamma}$  (red) shows a linear trend. Inset, the expected density of states (DOS) of a helical Dirac cone, which is 1/2 that of a graphene Dirac cone due to its single spin degeneracy. **g**, Schematic of the chiral Dirac fermion ground state of graphene, which exhibits spin-degenerate Dirac cones that intersect away from the Kramers' points. **h**, Schematic of the helical Dirac fermion ground state of  $\text{Bi}_{2-\delta}\text{Ca}_\delta\text{Se}_3$ ,  $\text{NO}_2$ , which exhibits a spin-polarized Dirac cone that intersects at a Kramers' point and guarantees a  $\nu_0 = 1$  topological order quantum number for the nodal Dirac ground state.

interactions between Dirac fermions of opposite helicity; this would enable searching for exotic quantum phenomena beyond the standard model of particle physics<sup>30</sup>.

## METHODS SUMMARY

Spin-integrated ARPES data were taken at beamlines 12.0.1 and 7.0.1 of the Advanced Light Source in Lawrence Berkeley National Laboratory with 29-eV to 100-eV photons. Typical energy and momentum resolutions were 15 meV and 1% of the surface Brillouin zone (29-eV photons) and 50 meV and 2% of the surface Brillouin zone (100-eV photons). Spin-resolved ARPES measurements were performed at the SIS beamline at the Swiss Light Source using the COPHEE spectrometer, which consists of two 40-kV classical Mott detectors that measure all three spatial components of spin polarization. Spin-resolved measurements were taken with 20-eV to 22-eV photons with energy and momentum resolutions of 80 meV and 3% of the surface Brillouin zone (all photons). Spin-integrated data were collected on tuned Bi<sub>2- $\delta$</sub> Ca <sub>$\delta$</sub> Se<sub>3</sub> and tuned Bi<sub>2</sub>Te<sub>3</sub> single crystals cleaved in ultrahigh vacuum (pressures better than  $5 \times 10^{-11}$  torr) and maintained at a temperature of 10 K unless otherwise specified. Spin-resolved data were collected at 50 K. Adsorption of NO<sub>2</sub> molecules on Bi<sub>2- $\delta$</sub> Ca <sub>$\delta$</sub> Se<sub>3</sub> was achieved via controlled exposures to NO<sub>2</sub> gas (Matheson, 99.5%). The adsorption effects were studied under static flow mode by exposing the cleaved sample surface to the gas for a certain time then taking data after the chamber was pumped down to the base pressure. Spectra of the NO<sub>2</sub> adsorbed surfaces were taken within minutes of opening the photon shutter to minimize photon exposure related effects. The theoretical band calculations were performed with the LAPW method in slab geometry using the WIEN2K package.

**Full Methods** and any associated references are available in the online version of the paper at [www.nature.com/nature](http://www.nature.com/nature).

Received 30 April; accepted 29 June 2009.

Published online 20 July 2009.

- Day, C. Exotic spin textures show up in diverse materials. *Phys. Today* **62**, 12–13 (2009).
- Moore, J. E. Topological insulators: the next generation. *Nature Phys.* **5**, 378–380 (2009).
- Fu, L., Kane, C. L. & Mele, E. J. Topological insulators in three dimensions. *Phys. Rev. Lett.* **98**, 106803 (2007).
- Qi, X.-L., Hughes, T. L. & Zhang, S.-C. Topological field theory of time-reversal invariant insulators. *Phys. Rev. B* **78**, 195424 (2008).
- Schnyder, A. P. *et al.* Classification of topological insulators and superconductors. *Phys. Rev. B* **78**, 195125 (2008).
- Essin, A., Moore, J. E. & Vanderbilt, D. Magnetoelectric polarizability and axion electrodynamics in crystalline insulators. *Phys. Rev. Lett.* **102**, 146805 (2009).
- Fu, L. & Kane, C. L. Probing neutral Majorana fermion edge modes with charge transport. *Phys. Rev. Lett.* **102**, 216403 (2009).
- Akhmerov, A. R., Nilsson, J. & Beenakker, C. W. J. Electrically detected interferometry of Majorana fermions in a topological insulator. *Phys. Rev. Lett.* **102**, 216404 (2009).
- Seradjeh, B., Moore, J. E. & Franz, M. Exciton condensation and charge fractionalization in a topological insulator film. Preprint at (<http://arxiv.org/abs/0902.1147>) (2009).
- Geim, A. K. & Novoselov, K. S. The rise of graphene. *Nature Mater.* **6**, 183–191 (2007).
- Li, L. *et al.* Phase transitions of Dirac electrons in bismuth. *Science* **321**, 547–550 (2008).
- Moore, J. E. & Balents, L. Topological invariants of time-reversal-invariant band structures. *Phys. Rev. B* **75**, 121306(R) (2007).
- Hsieh, D. *et al.* A topological Dirac insulator in a quantum spin Hall phase. *Nature* **452**, 970–974 (2008).
- Hsieh, D. *et al.* Observation of unconventional quantum spin textures in topological insulators. *Science* **323**, 919–922 (2009).
- Xia, Y. *et al.* Observation of a large-gap topological-insulator class with a single Dirac cone on the surface. *Nature Phys.* **5**, 398–402 (2009).

- Hor, Y. S. *et al.* p-type Bi<sub>2</sub>Se<sub>3</sub> for topological insulator and low-temperature thermoelectric applications. *Phys. Rev. B* **79**, 195208 (2009).
- Noh, H.-J. *et al.* Spin-orbit interaction effect in the electronic structure of Bi<sub>2</sub>Te<sub>3</sub> observed by angle-resolved photoemission spectroscopy. *Europhys. Lett.* **81**, 57006 (2008).
- Nishide, A. *et al.* Direct mapping of the spin-filtered surface bands of a three-dimensional quantum spin Hall insulator. Preprint at (<http://arxiv.org/abs/0902.2251>) (2009).
- Checkelsky, J. G., Li, L. & Ong, N. P. Divergent resistance of the Dirac point in graphene: evidence for a transition in high magnetic field. *Phys. Rev. B* **79**, 115434 (2009).
- Zhang, H. *et al.* Topological insulators in Bi<sub>2</sub>Se<sub>3</sub>, Bi<sub>2</sub>Te<sub>3</sub> and Sb<sub>2</sub>Te<sub>3</sub> with a single Dirac cone on the surface. *Nature Phys.* **5**, 438–442 (2009).
- Meier, F., Dil, J. H., Lobo-Checa, J., Patthey, L. & Osterwalder, J. Quantitative vectorial spin analysis in angle-resolved photoemission: Bi/Ag(111) and Pb/Ag(111). *Phys. Rev. B* **77**, 165431 (2008).
- Larson, P. *et al.* Electronic structure of Bi<sub>2</sub>X<sub>3</sub> (X = S, Se, Te) compounds: comparison of theoretical calculations with photoemission studies. *Phys. Rev. B* **65**, 085108 (2001).
- Mishra, S. K., Satpathy, S. & Jepsen, O. Electronic structure and thermoelectric properties of bismuth telluride and bismuth selenide. *J. Phys. Condens. Matter* **9**, 461–470 (1997).
- Urazhdin, S. *et al.* Surface effects in layered semiconductors Bi<sub>2</sub>Se<sub>3</sub> and Bi<sub>2</sub>Te<sub>3</sub>. *Phys. Rev. B* **69**, 085313 (2004).
- Black, J., Conwell, E. M., Seigle, L. & Spencer, C. W. Electrical and optical properties of some M<sub>2</sub><sup>V-B</sup>N<sub>3</sub><sup>VI-B</sup> semiconductors. *J. Phys. Chem. Solids* **2**, 240–251 (1957).
- Thomas, G. A. *et al.* Large electron-density increase on cooling a layered metal: doped Bi<sub>2</sub>Te<sub>3</sub>. *Phys. Rev. B* **46**, 1553–1556 (1992).
- Zhou, S. *et al.* Metal to insulator transition in epitaxial graphene induced by molecular doping. *Phys. Rev. Lett.* **101**, 086402 (2008).
- Schedin, F. *et al.* Detection of individual gas molecules adsorbed on graphene. *Nature Mater.* **6**, 652–655 (2007).
- König, M. *et al.* Quantum spin Hall insulator state in HgTe quantum wells. *Science* **318**, 766–770 (2007).
- Wilczek, F. Remarks on dyons. *Phys. Rev. Lett.* **48**, 1146–1149 (1982).

**Supplementary Information** is linked to the online version of the paper at [www.nature.com/nature](http://www.nature.com/nature).

**Acknowledgements** We acknowledge the following people for discussions: P. W. Anderson, B. Altshuler, L. Balents, M. R. Beasley, B. A. Bernevig, C. Callan, J. C. Davis, H. Fertig, E. Fradkin, L. Fu, D. Gross, D. Haldane, K. Le Hur, B. I. Halperin, D. A. Huse, C. L. Kane, C. Kallin, E. A. Kim, R. B. Laughlin, D.-H. Lee, P. A. Lee, J. E. Moore, A. J. Millis, A. H. Castro Neto, J. Orenstein, P. Phillips, S. Sachdev, Dan C. Tsui, A. Vishwanath, F. Wilczek, X.-G. Wen and A. Yazdani. The spin-resolved and spin-integrated ARPES measurements using synchrotron X-ray facilities and theoretical computations are supported by the Basic Energy Sciences of the US Department of Energy (DE-FG-02-05ER46200, AC03-76SF00098 and DE-FG02-07ER46352) and by the Swiss Light Source, Paul Scherrer Institute. Materials growth and characterization are supported by the NSF through the Princeton Center for Complex Materials (DMR-0819860) and Princeton University. M.Z.H. acknowledges additional support from the A. P. Sloan Foundation, an R. H. Dicke fellowship research grant and the Kavli Institute of Theoretical Physics at Santa Barbara.

**Author Contributions** D.H., Y.X. and D.Q. contributed equally to the experiment with the assistance of L.W. and M.Z.H.; D.G., Y.S.H. and R.J.C. provided critically important high quality single crystal samples; J.G.C. and N.P.O. performed the transport measurements; J.H.D., F.M., J.O., L.P. and A.V.F. provided beamline assistance; H.L. and A.B. carried out the theoretical calculations; M.Z.H. conceived the design to reach the topological transport regime and was responsible for the overall project direction, planning, and integration among different research units.

**Author Information** Reprints and permissions information is available at [www.nature.com/reprints](http://www.nature.com/reprints). Correspondence and requests for materials should be addressed to M.Z.H. ([mzhasan@Princeton.edu](mailto:mzhasan@Princeton.edu)).

## METHODS

**Spin-ARPES methods.** Spin-integrated angle-resolved photoemission spectroscopy (ARPES<sup>31</sup>) measurements were performed with 29–100 eV linearly polarized photons on beam lines 12.0.1 and 7.0.1 at the Advanced Light Source in Lawrence Berkeley National Laboratory. All endstations were equipped with a Scienta hemispherical electron analyser (see VG Scienta manufacturer website (<http://www.vgscienta.com/>) for instrument specifications). Spin-resolved ARPES measurements were performed at the SIS beam line at the Swiss Light Source using the COPHEE spectrometer<sup>32</sup> with two 40-kV classical Mott detectors and linearly polarized photons with energies of 20–22 eV. The COPHEE spectrometer is capable of measuring all three spatial components of the spin polarization vector for any point in reciprocal space, from which a spin-resolved band structure is constructed. The typical energy and momentum resolution was 15 meV and 1% of the surface Brillouin zone respectively at beam line 12.0.1, 50 meV and 2% of the surface Brillouin zone respectively at beam line 7.0.1, and 80 meV and 3% of the surface Brillouin zone respectively at SIS using a pass energy of 3 eV. Spin-integrated data were taken from single crystal Bi<sub>2- $\delta$</sub> Ca <sub>$\delta$</sub> Se<sub>3</sub> and Bi<sub>2</sub>Te<sub>3</sub> cleaved along its (111) surface in ultrahigh vacuum at pressures better than  $5 \times 10^{-11}$  torr and maintained at a temperature of 10 K unless otherwise specified. Spin-resolved data were collected at 50 K. Adsorption of NO<sub>2</sub> molecules on Bi<sub>2- $\delta$</sub> Ca <sub>$\delta$</sub> Se<sub>3</sub> was achieved via controlled exposures to NO<sub>2</sub> gas (Matheson, 99.5%). The adsorption effects were studied under static flow mode by exposing the cleaved sample surface to the gas for a certain time then taking data after the chamber was pumped down to the base pressure. Spectra of the NO<sub>2</sub> adsorbed surfaces were taken within minutes of opening the photon shutter to minimize potential photon induced charge transfer and desorption effects.

**Crystal growth methods.** To grow single crystals of Bi<sub>2- $\delta$</sub> Ca <sub>$\delta$</sub> Se<sub>3</sub>, a mixture of elemental Bi (99.999%) and Se (99.999%) was first melted at 800 °C in a quartz tube for 16 h, then cooled to room temperature. Stoichiometric amounts of Ca pieces (99.8%) were then added to the mixture and reheated to 400 °C for 16 h. After an additional day of heating at 800 °C, the crystalline sample was cooled to 550 °C in 24 h. The sample was then annealed for 3 days at 550 °C followed by furnace-cooling to room temperature. Scanning tunnelling microscopy data<sup>16</sup> has shown that Ca addition suppresses Se vacancies to a higher degree than the addition of excess Se alone. Large single crystals of Bi<sub>2</sub>Te<sub>3</sub> were grown by melting stoichiometric mixtures of elemental Bi (99.999%) and Te (99.999%) at 800 °C overnight in a sealed vacuum quartz tube. The crystalline sample was cooled over a period of two days to 550 °C, and maintained at the temperature for 5 days. It was then furnace cooled to room temperature.

**Sample quality characterization.** X-ray diffraction measurements were used to check that the samples were single phase, and confirmed that the single crystals presented in this paper have a rhombohedral crystal structure with space group  $D_{3d}^5(R\bar{3}m)$ . The X-ray diffraction patterns of the cleaved crystals exhibit only the ( $hhh$ ) peaks showing that the naturally cleaved surface is oriented along the trigonal (111) axis. Room temperature data were recorded on a Bruker D8 diffractometer using Cu K $\alpha$  radiation ( $\lambda = 1.54 \text{ \AA}$ ) and a diffracted beam monochromator. The crystal structure of Bi<sub>2</sub>(Te/Se)<sub>3</sub> can be visualized as a stack of hexagonal atomic layers, each consisting of only Bi or Te/Se. Five atomic layers are stacked in a close-packed f.c.c. fashion along the [111] direction in order Te/Se(1)-Bi-Te/Se(2)-Bi-Te/Se(1), in a quintuple layer, and cleavage takes place naturally between such layers. The topmost layer after cleavage is the Te/Se(1) layer as shown by scanning tunnelling microscopy data<sup>24</sup>. Our ARPES results were reproducible over many different sample batches, although relaxation time scales may vary by up to 10 min and the magnitude of band bending may vary up to 50 meV. The in-plane crystal orientation was determined by Laue X-ray diffraction before insertion into an ultrahigh vacuum environment. Cleaving these samples *in situ* between 10 K and 300 K at chamber pressures less than  $5 \times 10^{-11}$  torr resulted in shiny flat surfaces.

**Bulk transport measurements.** Resistivity and Hall effect measurements were done in standard four-probe geometries with an AC applied current at 18 Hz. Current was applied in the  $a$ - $b$  plane and magnetic field along the  $c$ -axis ([111] direction) for Hall effect measurements. Contacts were made with gold wire and silver paint, with resulting contact resistance less than 1  $\Omega$ . Measurements were done under vacuum pressures better than  $10^{-6}$  torr.

**Theoretical band calculation methods.** The calculations were performed with the LAPW method in slab geometry using the WIEN2K package<sup>33</sup>. Generalized gradient approximations<sup>34</sup> were used to describe the exchange-correlation potential. Spin-orbit coupling was included as a second variational step using scalar-relativistic eigenfunctions as basis. The surface was simulated by placing a slab of six quintuple layers in vacuum using optimized lattice parameters<sup>35</sup>. A grid of  $35 \times 35 \times 1$  points were used in the calculations, equivalent to 120  $k$ -points in the irreducible Brillouin zone and 2,450  $k$ -points in the first Brillouin zone.

31. Hufner, S. *Photoelectron Spectroscopy* (Springer, 1995).
32. Hoesch, M. *Spin-polarized Fermi Surface Mapping*. PhD thesis, Univ. Zurich (2002).
33. Blaha, P. et al. *Computer Code WIEN2k* (Vienna University of Technology, 2001).
34. Perdew, J. P., Burke, K. & Ernzerhof, M. Generalized gradient approximation made simple. *Phys. Rev. Lett.* **77**, 3865–3868 (1996).
35. Wang, G. & Cagin, T. Electronic structure of the thermoelectric materials Bi<sub>2</sub>Te<sub>3</sub> and Sb<sub>2</sub>Te<sub>3</sub> from first-principles calculations. *Phys. Rev. B* **76**, 075201 (2007).